




# The photocatalytic performance of ternary g-C<sub>3</sub>N<sub>4</sub>/Bi<sub>2</sub>O<sub>3</sub>/TiO<sub>2</sub> heterojunction composite for degradation of organic pollutants under visible and ultraviolet light

Chengwei Zhong<sup>1,2</sup>, Wei Wei<sup>1,2</sup>, Huan He<sup>1,2</sup>, Zhuoxi Huangfu<sup>1,2</sup>, YiZheng Wang<sup>1</sup>, and Jiang Yu<sup>1,2,\*</sup> 

<sup>1</sup>Department of Environmental Science and Engineering, College of Architecture and Environment, Sichuan University, No. 24 South Section 1, Yihuan Road, Chengdu 610065, People's Republic of China

<sup>2</sup>Institute of New Energy and Low Carbon Technology, Sichuan University, Chengdu 610065, People's Republic of China

Received: 14 August 2020

Accepted: 26 November 2020

Published online:  
2 January 2021

© The Author(s), under exclusive licence to Springer Science+Business Media, LLC part of Springer Nature 2021

## ABSTRACT

Heterojunction photocatalytic materials have received extensive attention by the researchers. In this work, g-C<sub>3</sub>N<sub>4</sub>/Bi<sub>2</sub>O<sub>3</sub>/TiO<sub>2</sub> (TCB) composites with g-C<sub>3</sub>N<sub>4</sub> as the main body were synthesized via microwave-assisted ball milling and the heat treatment method. The photocatalytic activity was evaluated by the degradation efficiency of rhodamine B (RhB) and methylene blue (MB) under visible or UV light irradiation. TCB with a mass ratio of melamine/TiO<sub>2</sub>/Bi(NO<sub>3</sub>)<sub>3</sub>·5H<sub>2</sub>O of 30:1:0.25 has the best photocatalytic performance when fabricated at 450 °C in open air, and the degradation efficiency of the as-prepared material to RhB was 48.07% under visible light and 51.18% to MB under UV. The results of morphological structure analysis revealed that there was a flocculent structure on the edge of the g-C<sub>3</sub>N<sub>4</sub> film and the phase of TiO<sub>2</sub> and Bi<sub>2</sub>O<sub>3</sub> changed. The presence of β-Bi<sub>2</sub>O<sub>3</sub> enhanced photocatalytic efficiency of the as-prepared materials. The optical properties analysis confirmed that the structure of the hybrid samples can promote electron–hole pairs separately at multilayer heterogeneous interfaces and the electron can react with O<sub>2</sub> to yield the ·O<sub>2</sub><sup>-</sup> radical. In summary, the ability of novel spatial structure materials to absorb visible light is enhanced, which are facilitated for photocatalytic activity and have excellent stability. Therefore, the study of ternary heterojunction photocatalytic materials provides a reference for environmental remediation.

Address correspondence to E-mail: yuj@scu.edu.cn

## 1 Introduction

Heterojunction photocatalytic materials which can be classified into Type-I [1], Type-II [2], and Z-scheme type [3] according to the electron–hole pairs transmission mechanism are used in the field of environmental remediation. It not only can directly adsorb sunlight to generate a large number of electron–hole pairs but also can yield active radicals for the oxidation of refractory organic pollutants [4–6].  $\text{TiO}_2$  has been used as a typical photocatalytic material for a long time [7, 8]. In recent years,  $g\text{-C}_3\text{N}_4$  formed by the melamine thermal polymerization reaction has outstanding properties and has become a research focus in the field of photocatalysis [9]. Conventional photocatalytic materials have certain limitations and then launched the study of binary heterojunction. Related research has proven that  $\text{TiO}_2$ -based heterojunction photocatalytic materials prepared by the sol–gel method have a better degradation effect on pollutants, such as methyl green and methyl orange, under visible light [10, 11], and others methods to synthesize  $\text{TiO}_2/g\text{-C}_3\text{N}_4$  composites for degradation organic pollutants have been reported [12–14]. Despite the binary heterojunction photocatalytic materials based on  $\text{TiO}_2$  or  $g\text{-C}_3\text{N}_4$  have exhibited potential capabilities in environmental remediation, the responses of  $\text{TiO}_2/g\text{-C}_3\text{N}_4$  composites to sunlight were not as desirable, because the experiments were usually tested under visible light. [15–18].

To further improve the photocatalytic activity of the materials, the modification methods of ternary or multiple doped composite systems have attracted wide attention. Tahir et al. through hydrothermal method synthesized a novel ternary hybrid photocatalyst  $\text{WO}_3/\text{TiO}_2/g\text{-C}_3\text{N}_4$  which have excellent structure and extend surface area were beneficial to the visible light absorption capacity and photocatalytic activity. The removal efficiency of acetylsalicylate and methylthiobromine could reach 98% and 97%, respectively [19]. 3D structure  $g\text{-C}_3\text{N}_4/\text{TiO}_2/\text{kaolinite}$  composite exhibited degradation ability for the removal of ciprofloxacin (CIP) under visible light irradiation [20], but the ternary heterojunction material absorption range of light is not wide enough. Zhang et al. prepared  $g\text{-C}_3\text{N}_4/\text{Bi}_2\text{O}_3/\text{TiO}_2$  nanotube photocatalytic material electrodes by anodization [21], and the degradation efficiency to MB reached 77.5% after 3 h of photoelectron catalysis,

demonstrating the ternary heterojunction materials have development potential in photocatalyst. There are few research reports on  $g\text{-C}_3\text{N}_4/\text{Bi}_2\text{O}_3/\text{TiO}_2$  heterojunction photocatalytic materials. Bismuth oxide ( $\text{Bi}_2\text{O}_3$ ) as bismuth-based catalysts is a new type of nano-semiconductor material which has been widely studied in the field of photocatalysis due to its narrow band gap (2.8 eV), high surface area, and exposed active crystal plane [22–26]. Simultaneously, the responses of  $\text{Bi}_2\text{O}_3$  to UV and visible light are excellent [27].

Previous studies have demonstrated that  $g\text{-C}_3\text{N}_4/\text{TiO}_2$  (TCN) hybrid photocatalytic materials which can be decided to Z-scheme electron–hole transfer model showed improved photocatalytic efficiency in degrading simulated pollutants under visible light irradiation [28]. Based on previous study, we plan to dope a certain amount of  $\text{Bi}(\text{NO}_3)_3 \cdot 5\text{H}_2\text{O}$  to prepare a novel spatial structure heterojunction photocatalytic material  $g\text{-C}_3\text{N}_4/\text{Bi}_2\text{O}_3/\text{TiO}_2$  (TCB) via microwave-assisted ball milling and the heat treatment method. In this work, the composite materials of doping  $\text{Bi}_2\text{O}_3$  have potential to enhance the UV and visible light absorption ability, improve separation, and transfer efficiency of photogenerated charges, and yield more active radicals to degrade organic pollutants. The efficiency of TCB to degrade RhB and MB under visible or UV light was studied. A series of characterization methods were used to detect the structural properties and optical properties of composites, and combined with free radical capture experiment to the photocatalytic mechanism was further explored.

## 2 Materials and methods

### 2.1 Reagent

Titanium dioxide ( $\text{TiO}_2$ ) was provided by Xuan-Cheng JingRui New Material Co. Ltd. Other chemical reagents melamine, bismuth nitrate pentahydrate ( $\text{Bi}(\text{NO}_3)_3 \cdot 5\text{H}_2\text{O}$ ), Rhodamine B (RhB), Methylene blue (MB), Benzoquinone (BQ), Isopropanol (IPA), and Ammonium oxalate (AO) were obtained from Aladdin Chemistry Co. Ltd. All of the reagents were of analytical purity and used without further purification. Deionized water was produced in an Ultra-pure water system for laboratory use (WP-UP-1810).

## 2.2 Experimental methods

### 2.2.1 Preparation of $g\text{-C}_3\text{N}_4$ and $\text{Bi}_2\text{O}_3$

An appropriate amount of melamine was placed in a muffle furnace (SX2-2.5-10, Zhengzhou, China) under atmospheric air and heated to 500 °C at a rate of 5 °C  $\text{min}^{-1}$ , then steadied at 500 °C for 2 h. The resulting yellow solid was ground into powder in an agate mortar after cooling down to room temperature. The final product was  $g\text{-C}_3\text{N}_4$ .  $\text{Bi}_2\text{O}_3$  was prepared at the same process under 450 °C, which was collected for further use.

### 2.2.2 Synthesis of $g\text{-C}_3\text{N}_4/\text{Bi}_2\text{O}_3/\text{TiO}_2$

The synthesis of TCB involved four steps: (1) An appropriate amount of  $\text{Bi}(\text{NO}_3)_3 \cdot 5\text{H}_2\text{O}$  was mixed with TNC (mass ratio of melamine/ $\text{TiO}_2$  30: 1), and the outstanding photocatalytic material in previous research was obtained [28]. The mixture was added into an agate ball milling tank (PM2L, Nanjing, China), with a ball:material ratio of 10:1, and deionized water was used as the dispersant. A uniform heterogeneous interface was obtained in the ball milling tank after 2–3 h at a speed of 400 rpm. (2) The suspension was heated in a microwave oven at 700 W for 20–30 min after milling to prepare the crystal structure and heterojunction material. (3) The faint yellow material was further milled in an agate mortar, and after the molecular structure reached thermal equilibrium it was placed in room temperature for 2–3 h. (4) The sample was placed in a muffle furnace under atmospheric air and heated up to 450 °C at a rate of 5 °C  $\text{min}^{-1}$ , then steadied for 2 h. The as-synthesized material was obtained after regrinding in an agate mortar. The different hybrid composites with mass ratios of melamine/ $\text{TiO}_2$ / $\text{Bi}(\text{NO}_3)_3 \cdot 5\text{H}_2\text{O}$  at 30:1:0.1, 30:1:0.25, 30:1:0.5, 30:1:1, 30:1:5, 30:1:10, 30:1:20, and 30:1:30 were labeled TCB-1, TCB-2, TCB-3, TCB-4, TCB-5, TCB-6, TCB-7, and TCB-8, respectively.

## 2.3 Characterizations

An X-ray diffractometer (XRD) (Empyrean, Shimadzu, Japan) with Cu-K radiation ( $\lambda = 0.15405$  nm, 60 kV, 60 mA) was used to determine the sample crystal structure. X-ray photoelectron spectroscopy (XPS) was performed using Escalab 250Xi system

(Thermo Fisher, America) analysis to determine the element composition of the sample. The sample surface morphology structure and element content were detected by a JSM-7500F (JEOL, Japan) scanning electron microscope (SEM) and energy dispersive spectrometer (EDS), respectively. The internal microstructure of the sample was observed by transmission electron microscopy (TEM). The optical performance was detected by UV–Vis diffuse reflectance spectra (DRS) equipped with a UV-3600 (Shimadzu, Japan) spectrophotometer. Photoluminescence (PL) emission spectra were detected on a Fluorescence Spectrometer (F-7000, Hitachi, Japan), and the excitation wavelength was 230–900 nm. The photoreactor is shown in Fig. 1

## 2.4 Photocatalytic performance tests

The photocatalytic performance of the as-obtained samples was determined by the degradation of RhB and MB, with an initial concentration of 20.0  $\text{mg L}^{-1}$ , under both UV and visible light irradiation. Reaction systems consisted of 50 mg catalysts (TCB,  $\text{TiO}_2$ ,



**Fig. 1** The photoreactor of this experiment

g-C<sub>3</sub>N<sub>4</sub>, Bi<sub>2</sub>O<sub>3</sub>) and 50.0 mL of simulated dye wastewater in 100 mL beakers. The mixtures were dispersed by ultrasound for 5 min and stirred in a magnetic stirrer for 30 min with darkroom conditions. The first sample was taken when the adsorption–desorption reached dynamic equilibrium. Afterwards, a 5 mL sample was centrifuged at 10,000 rpm for 20 min after reacting in UV or visible light irradiation for 60 min each. The supernatant solution was analyzed by Alpha-1506 UV–vis spectroscopy (Shanghai Lab-Spectrum Instruments Co. Ltd., China) in which the visible light was 60 W 460 nm LED tube and UV was 60 W 254 nm tube at wavelengths of 554 nm and 664 nm for RhB and MB, respectively, and the average light intensity is 50 mW/cm<sup>2</sup>.

The degradation efficiency of simulated pollutants can be calculated using Eq. (1):

$$\eta = \left[ \frac{(C_0 - C_t)}{C_0} \right] \times 100\% \quad (1)$$

In the equation,  $\eta$  is the removal rate of the simulated pollutants;  $C_0$  is the initial simulated pollutant concentration; and  $C_t$  is the concentration of simulated pollutants after reacting  $t$  min.

In this experiment, the scavengers BQ, IPA, and AO were employed to capture superoxide anion radical ( $\cdot O_2^-$ ), hydroxyl radicals ( $\cdot OH$ ), and photo-generated hole ( $h^+$ ) [29]. 50.0 mg TCB-2 and 50 mL RhB were added into 4 100 mL dry and transparent beakers and labeled 1–4, respectively. 2–4 sign beakers were added 1 mL (0.1 mM) scavenger of BQ, IPA, and AP, respectively [24, 30].

## 3 Results and discussion

### 3.1 XRD pattern

Figure 2 shows that Bi<sub>2</sub>O<sub>3</sub> was the product of Bi(NO<sub>3</sub>)<sub>3</sub>·5H<sub>2</sub>O direct thermal decomposition through comparing the XRD patterns of Bi<sub>2</sub>O<sub>3</sub> with the PDF#71-0465 standard pattern. It was further found that the XRD peaks of g-C<sub>3</sub>N<sub>4</sub> were in TCB-2 with no obvious XRD diffraction peaks of anatase phase TiO<sub>2</sub>. On the contrary, the rutile phase TiO<sub>2</sub> can be observed when referred to the PDF#21–1272 standard pattern. It demonstrates that the anatase phase TiO<sub>2</sub> is transformed into the rutile phase in the sample TCB-2. In addition, Bi<sub>2</sub>O<sub>3</sub> has four crystallographic

polymorphs with monoclinic- $\alpha$ , body-centered cubic- $\gamma$ , tetragonal- $\beta$ , and face-centered cubic- $\delta$  [31]. The  $\alpha$ -Bi<sub>2</sub>O<sub>3</sub>, originally generated from Bi(NO<sub>3</sub>)<sub>3</sub>·5H<sub>2</sub>O, is converted into  $\beta$ -Bi<sub>2</sub>O<sub>3</sub> because the peaks belonging to  $\beta$ -Bi<sub>2</sub>O<sub>3</sub> can be observed in TCB-2 [32]. The formation temperature of  $\beta$ -Bi<sub>2</sub>O<sub>3</sub> and the rutile phase TiO<sub>2</sub> are higher than  $\alpha$ -Bi<sub>2</sub>O<sub>3</sub> and the anatase phase TiO<sub>2</sub> [33], implying that the change of the crystal phase of TiO<sub>2</sub> and Bi<sub>2</sub>O<sub>3</sub> may be caused by exothermic reaction [34, 35]. On the other hand, the deamination and dehydrogenation of melamine impacted on the chemical bond of TiO<sub>2</sub> and Bi<sub>2</sub>O<sub>3</sub> and induced the change of the crystal phase. From the above comparative analysis, we can identify the sample of TCB-2 as containing the rutile phase TiO<sub>2</sub>, g-C<sub>3</sub>N<sub>4</sub>, and  $\beta$ -Bi<sub>2</sub>O<sub>3</sub>. In addition, the synthesis materials have good crystallinity due to the sharp shaped peaks observed.

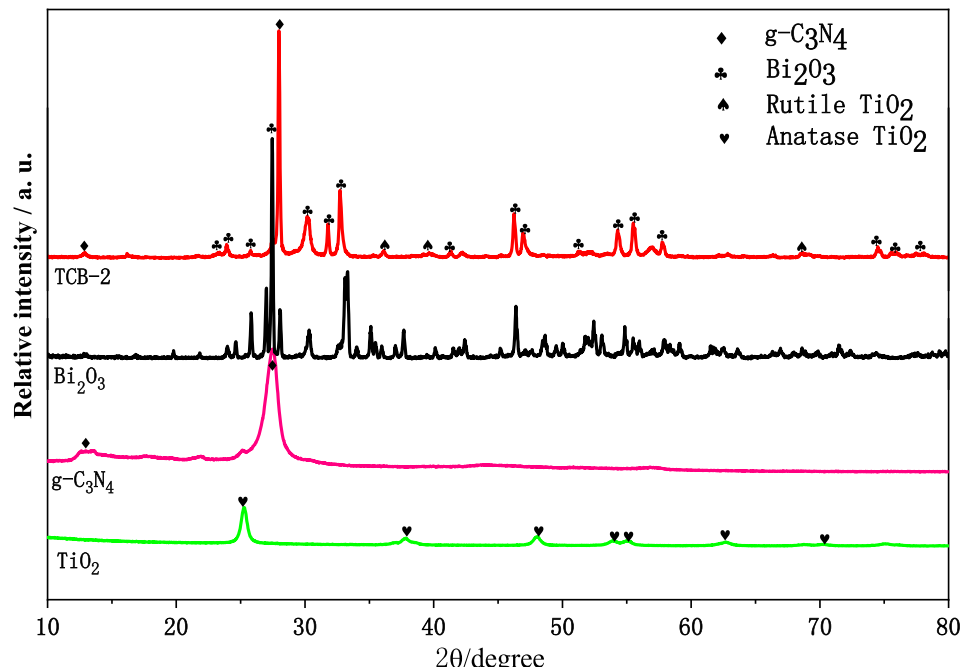
### 3.2 XPS analysis

The XPS spectra were used to further probe the chemical compositions and chemical bonds in TCB-2. Figure 3 shows the XPS peak spectrum of five elements: carbon (C), nitrogen (N), titanium (Ti), bismuth (Bi), and oxygen (O) in TCB-2. Two peaks at 288.6 eV and 284.75 eV corresponding to sp<sup>2</sup>-bonded carbon (N=C=N) and C1s [36] are observed in Fig. 3a, respectively. As displayed in Fig. 3b, the peaks at 398.1 eV and 401.0 eV are ascribed to sp<sup>2</sup>-hybridized nitrogen (C=N=C) and N hydrogen bond (N–H) [37, 38], respectively. The XPS characteristic peaks of C and N elements indicate the presence of g-C<sub>3</sub>N<sub>4</sub> in TCB-2. This is consistent with the XRD results. Meanwhile, the peaks attributed to Ti 2p<sub>3/2</sub>, Ti 2p<sub>1/2</sub>, Bi 4d<sub>3</sub>, Bi 4f<sub>7/2</sub>, and Bi 4f<sub>5/2</sub>, respectively, can be determined from Fig. 3c and d [39, 40], respectively, suggesting the presence of TiO<sub>2</sub> and Bi<sub>2</sub>O<sub>3</sub> in TCB-2. Moreover, the peaks of Bi–O (528.3 eV), Ti–O (529.9 eV), and O–H (531.9 eV) in Fig. 3e [41], further confirm the existence of TiO<sub>2</sub> and Bi<sub>2</sub>O<sub>3</sub>. In the whole process, no evidence was found of chemical bonding between TiO<sub>2</sub>, g-C<sub>3</sub>N<sub>4</sub>, and Bi<sub>2</sub>O<sub>3</sub>, indicating the synthesis of TCB-2 was not by chemical means but by van der Waals forces or electrostatic adsorption.

### 3.3 SEM and TEM analysis

The nanoparticles of TiO<sub>2</sub> (Fig. 4a) and Bi<sub>2</sub>O<sub>3</sub> (Fig. 4b) were densely and uniformly attached to the film

**Fig. 2** XRD patterns of TiO<sub>2</sub>, g-C<sub>3</sub>N<sub>4</sub>, and TCB-2



formed by g-C<sub>3</sub>N<sub>4</sub>, and there was a flocculent structure on the edge of the g-C<sub>3</sub>N<sub>4</sub> film, the results may have been caused by exothermic reaction releasing heat that promoted polymerization between substances when adding Bi(NO<sub>3</sub>)<sub>3</sub>·5H<sub>2</sub>O in preparing hybrids during sintering of Bi<sub>2</sub>O<sub>3</sub> which increased the actual temperature. Thus, the film edge of g-C<sub>3</sub>N<sub>4</sub> produced by melamine changed into flocculent form. The as-prepared materials have formed the micro-nano structure, the size distribution was 0.4–3.0 μm. During the reaction, anatase phase TiO<sub>2</sub> in the raw material was gradually converted into the rutile phase TiO<sub>2</sub> which uniformly adhered to the g-C<sub>3</sub>N<sub>4</sub> film together with the Bi<sub>2</sub>O<sub>3</sub> formed by the decomposition of Bi(NO<sub>3</sub>)<sub>3</sub>·5H<sub>2</sub>O. Consequently, the TCB composite heterojunction materials with g-C<sub>3</sub>N<sub>4</sub> as the main body were formed. The EDS chart (Fig. 4c) revealed that the atomic ratio of C and N was close to 3: 4, demonstrating the g-C<sub>3</sub>N<sub>4</sub> was existence in TCB-2. The nanoparticles of TiO<sub>2</sub> and Bi<sub>2</sub>O<sub>3</sub> were uniformly attached to the film of g-C<sub>3</sub>N<sub>4</sub>, as can be observed from the multilayer structure of TCB-2 in Fig. 4d, 3e, 3f. Furthermore, comparing to the PDF#27-0050 standard pattern, it can be seen in Fig. 4e, 3f that two different lattice fringes of 0.248 nm and 0.346 nm correspond to the [101] crystal plane of rutile TiO<sub>2</sub>[42] and [210] crystal plane of Bi<sub>2</sub>O<sub>3</sub>, respectively. In summary, this was in

accordance with the analysis conclusions of XRD and XPS, further accounting for the rutile TiO<sub>2</sub> and Bi<sub>2</sub>O<sub>3</sub> nanoparticles uniformly attached to the surface of g-C<sub>3</sub>N<sub>4</sub>.

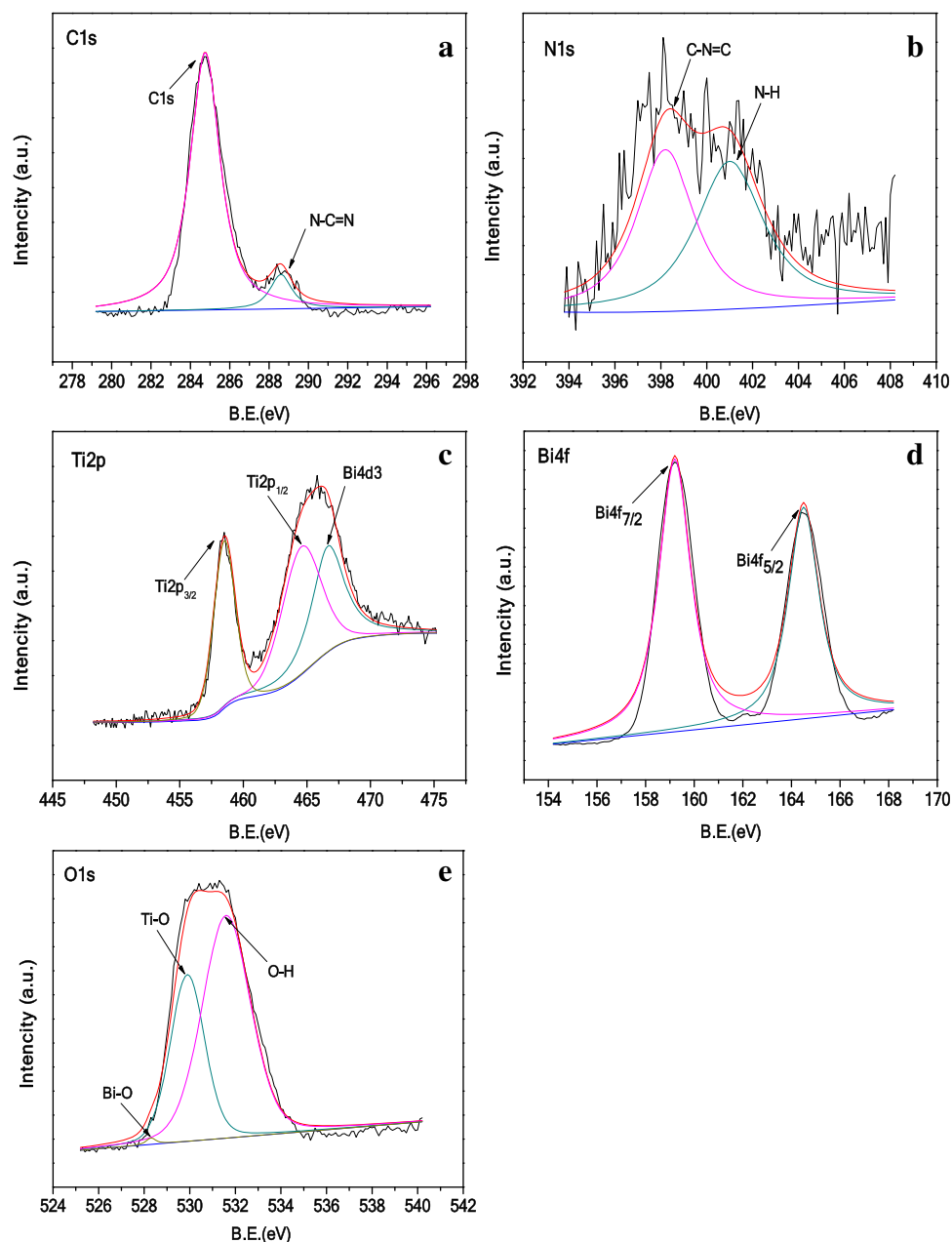
### 3.4 UV–vis diffuse reflection spectra

Figure 5 shows the UV–Vis diffuse reflectance spectra of TiO<sub>2</sub>, g-C<sub>3</sub>N<sub>4</sub>, Bi<sub>2</sub>O<sub>3</sub>, and TCB-2 at 200 to 800 nm and their corresponding Tauc plots. The light absorption range of TCB-2 was red-shifted relative to TiO<sub>2</sub>, Bi<sub>2</sub>O<sub>3</sub>, and g-C<sub>3</sub>N<sub>4</sub> (Fig. 5a) and exhibited a certain absorption in the visible light range at 200 to 500 nm. Equation (2) can be used to calculate the band gap energy of the photocatalysis [43]:

$$\alpha hv = A(hv - E_g)^{\frac{n}{2}} \quad (2)$$

In this equation,  $\alpha$ ,  $h$ ,  $v$ ,  $A$ , and  $E_g$  are absorption coefficient, Planck constant, light frequency, proportionality, and band gap energy, respectively;  $n$  represents the properties of the transition in a semiconductor ( $n = 1$  for direct transition, and  $n = 4$  for indirect transition). The  $\alpha$ -Bi<sub>2</sub>O<sub>3</sub> was an indirect transition, so the value of  $n$  was 4 [10]. From the tangents in Fig. 5b,  $E_g$  of Bi<sub>2</sub>O<sub>3</sub> and TCB-2 were 2.80 eV and 2.83 eV, respectively. The  $E_g$  of Bi<sub>2</sub>O<sub>3</sub> was similar to that of Cui et al. [41].

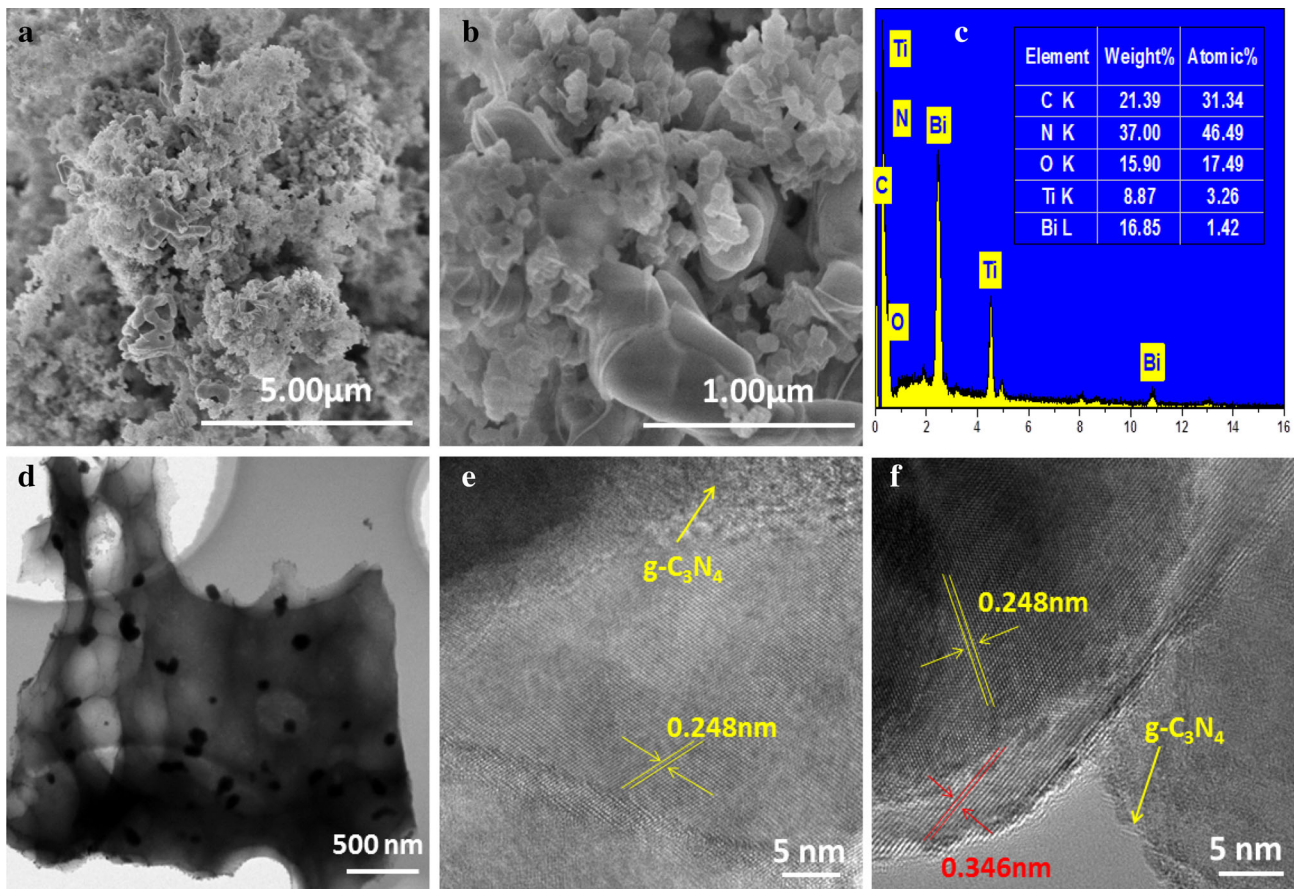
**Fig. 3** XPS spectra of C1s (a), N1s (b), Ti2p (c), Bi4f (d), and O1s (e) for TCB-2



### 3.5 Photocatalytic activity

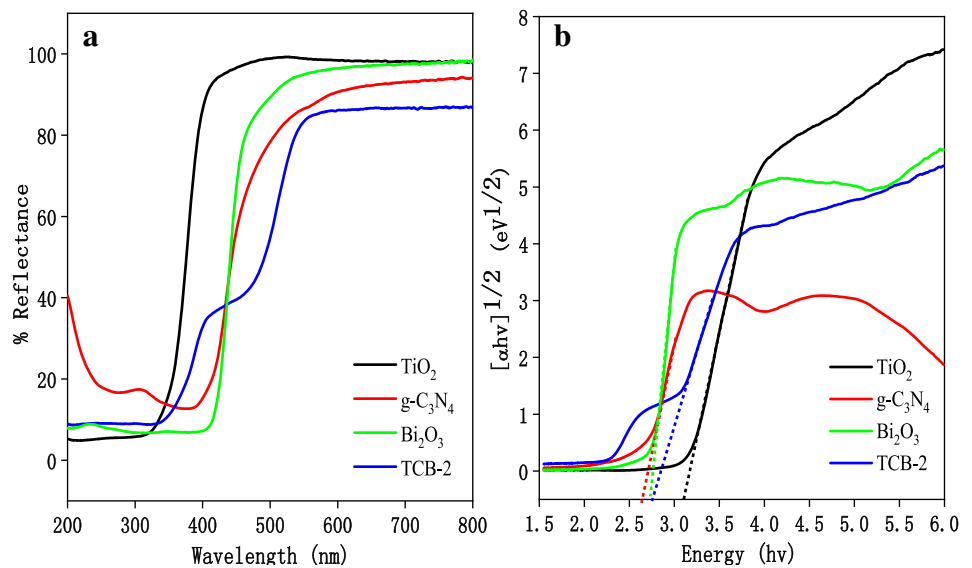
The results of the adsorption experiments performed in the dark are seen in Fig. 6. The adsorption capability of composites TCB to MB was better than RhB. TCB-7 had the best adsorption efficiency to MB reaching 8.82%, and the adsorption effect of samples for RhB was less than 2.5%. The adsorption capability of TCB was lower [28], demonstrating that the adding Bi<sub>2</sub>O<sub>3</sub> affects adsorption performance, and it is possible that TCB also has certain selective adsorption.

Figure 7 shows the degradation of RhB and MB for the 8 different ratios of TCB hybrid samples under visible light and UV irradiation after 240 min. TCB-2 has a better visible light absorption capacity compared with traditional photocatalytic material. In the series of composites, TCB-2 has the best photocatalytic effect in degrading RhB whether in visible light or UV irradiation. For visible light irradiation, the degradation efficiency of TCB-2 to RhB was only 48.07%, and it is lower than the efficiency of g-C<sub>3</sub>N<sub>4</sub> (99.36%). The degradation efficiency of TCB-2 to MB (40.10%) was lower than that of TiO<sub>2</sub> (63.31%) and



**Fig. 4** **a** and **b** SEM of TCB-2, **c** EDS of TCB-2, **d**, **e**, and **f** TEM of TCB-2

**Fig. 5** **a** UV–vis diffuse reflectance spectra of the photocatalysis and **b** their corresponding Tauc plots



$g\text{-C}_3\text{N}_4$  (89.78%). Under UV light irradiation, the degradation effect of TCB-7 on RhB was the best (68.66%), which was higher than that of  $\text{TiO}_2$  (63.64%), and the degradation effect of TCB-2 on MB

(51.18%) was not as good as  $\text{TiO}_2$  (91.39%). The above analysis clearly revealed that (1) the degradation effect of TCB under UV light was better than that of visible light; (2) the photocatalytic effect of TCB on

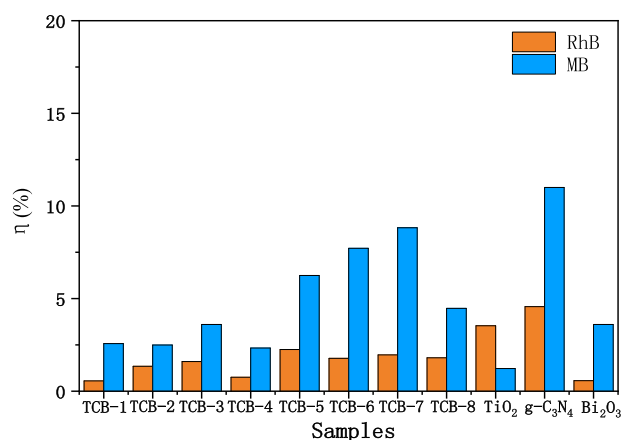


**Fig. 6** The adsorption efficiency of TCB samples for RhB and MB

RhB was slightly better than that of MB; (3) considering the irradiation, adsorption, and degradation three aspects, the comprehensive performance of TCB-2 was the best. Although the degradation effect of TCB-2 to 2 simulated pollutants were worse than the homogenous materials of TiO<sub>2</sub> and g-C<sub>3</sub>N<sub>4</sub>. On the one hand, it may have been caused by the fact that β-Bi<sub>2</sub>O<sub>3</sub> has the poor stability of thermodynamics in heterojunction interface [44], and the materials structure and photocatalytic system of TCB have been affected. On the other hand, it may also have been due to the selectivity and poor adsorption of TCB to pollutants resulting in a lower degradation efficiency. The DRS and other characterization analyses of TCB-2 showed that the hybrid material had a good response to visible light due to β-Bi<sub>2</sub>O<sub>3</sub> having an excellent absorption to visible light, lower band gap, and higher energy compared with α-Bi<sub>2</sub>O<sub>3</sub> [45, 46]. Therefore, this was further studied.

In order to investigate the reuse efficiency of hybrid materials, 50 mg TCB-2 samples were used to degrade simulated dye wastewater RhB and MB at a concentration of 20 mg L<sup>-1</sup>, and the number of times the photocatalytic material was recycled was investigated under visible light irradiation (Fig. 8). After 5 times of reuse, the degradation of RhB and MB by TCB-2 decreased from 51.91% and 40.63% to 45.46% and 36.04%, respectively. In general, the samples had a certain of photocatalytic stability.

### 3.6 Photocatalytic reaction mechanism

As we all know, the photoluminescence (PL) spectra had related to further reflect the electron–hole pairs

separation and transfer efficiency of semiconductors in the photocatalytic reactions [6, 47]. As Fig. 9 shows, the PL intensity of the pure TiO<sub>2</sub> was in the wavelength range between 360 and 540 nm, and has a strong emission peak at 426 nm. Obviously, there was a weaker PL peak than g-C<sub>3</sub>N<sub>4</sub>/TiO<sub>2</sub> for TCB-2, indicating that the electron–hole pairs recombination is slower than g-C<sub>3</sub>N<sub>4</sub>/TiO<sub>2</sub>. It is not difficult to understand that the ternary heterojunction TCB-2 exhibits an enhanced photocatalytic performance which can efficiently separate the photogenerated carries.

In order to prove the influence of active radicals in the system of TCB-2 degrading RhB under visible light irradiation, we added three scavengers BQ, AO, and IPA to study the free radical capture experiment. The removal efficiency at 240 min can reach 51.8%, after adding 1 mL BQ, IPA, and AO, the RhB removal efficiency promptly decreased to 5.3%, 14.3%, and 20.1%, respectively. As Fig. 10 shows, the material's photocatalytic efficiency was reduced and the degree of influence was BQ > IPA > AO, suggesting that ·O<sub>2</sub><sup>-</sup>, ·OH and h<sup>+</sup> were generated in the system, and that ·O<sub>2</sub><sup>-</sup> is the main active radical in RhB degradation process.

According to four conditions: (a) the analysis of DRS, (b) Eq. (3):  $E_{VB} = \chi - E_c + 0.5E_g$ , (c) Eq. (4):  $E_{CB} = E_{VB} - E_g$ , and (d) the  $\chi$  values for g-C<sub>3</sub>N<sub>4</sub>, TiO<sub>2</sub>, and Bi<sub>2</sub>O<sub>3</sub> were 4.73 eV, 5.81 eV, and 6.23 eV [6, 43, 47, 48]. We can calculate the conduction band and valence band of g-C<sub>3</sub>N<sub>4</sub>, TiO<sub>2</sub>, and Bi<sub>2</sub>O<sub>3</sub>, respectively, as shown in Table 1.

Based on the above results, we explored the composites g-C<sub>3</sub>N<sub>4</sub>/Bi<sub>2</sub>O<sub>3</sub>/TiO<sub>2</sub> photocatalytic degradation reaction mechanism for RhB and MB in visible light or UV irradiation. For visible light irradiation (Fig. 11a), in the hybrid mainly composed of g-C<sub>3</sub>N<sub>4</sub>, the electrons in the VB of g-C<sub>3</sub>N<sub>4</sub> and Bi<sub>2</sub>O<sub>3</sub> transferred to the corresponding CB, respectively. On account of the CB of g-C<sub>3</sub>N<sub>4</sub> has being more negative than that of Bi<sub>2</sub>O<sub>3</sub> and TiO<sub>2</sub>. The electrons in the CB of g-C<sub>3</sub>N<sub>4</sub> can cross the multilayer heterointerface and transfer to the CB of Bi<sub>2</sub>O<sub>3</sub> and TiO<sub>2</sub>, then reacting with O<sub>2</sub> to yield ·O<sub>2</sub><sup>-</sup> radical (− 0.33 eV) degrade RhB due to the E<sub>CB</sub> of g-C<sub>3</sub>N<sub>4</sub> was estimated to be − 1.12 eV. ·O<sub>2</sub><sup>-</sup> radicals can further react with electrons to yield H<sub>2</sub>O<sub>2</sub> and ·OH. The VB of Bi<sub>2</sub>O<sub>3</sub> (3.13) was more positive than that of g-C<sub>3</sub>N<sub>4</sub> (1.58), so the holes can migrate to Bi<sub>2</sub>O<sub>3</sub> owing to the different VB



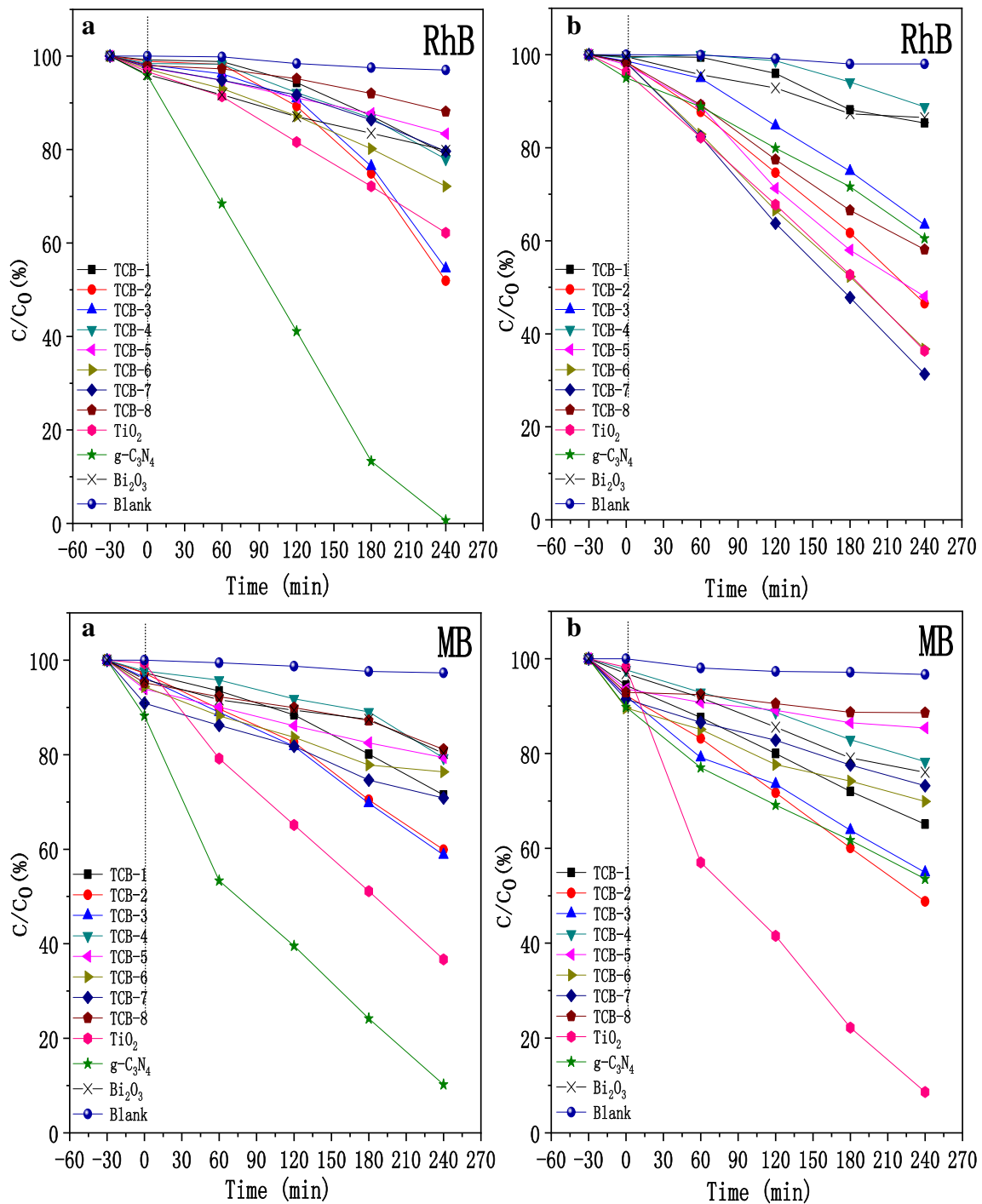


**Fig. 7** The degradation efficiency of TCB samples for RhB and MB after 240 min under **a** visible light and **b** UV light irradiation

edge potentials, and participate in photocatalytic reactions to directly or indirectly degrade RhB or MB.  $TiO_2$  played an important role in electrons transfer in this system, though it cannot be induced by visible light. The entire photocatalytic reaction system

realized the effective separation of the electron–hole pair to promote the photocatalytic ability. With UV irradiation (Fig. 11b), similarly,  $g-C_3N_4$ ,  $Bi_2O_3$  and  $TiO_2$  can be excited, respectively. Consequently, according to different band gap energy shown in

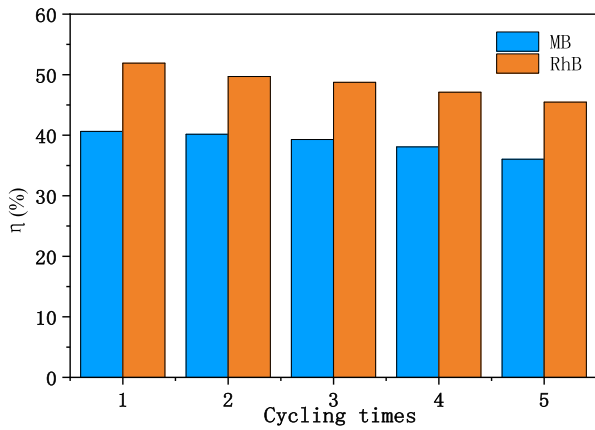


**Fig. 8** The degradation efficiency of RhB and MB by reused sample TCB-2 under visible light irradiation

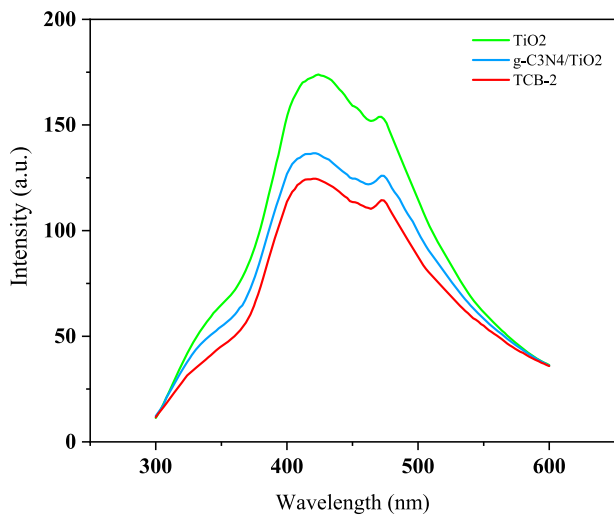


**Fig. 9** PL spectra of TiO<sub>2</sub>, g-C<sub>3</sub>N<sub>4</sub>/TiO<sub>2</sub> and TCB-2

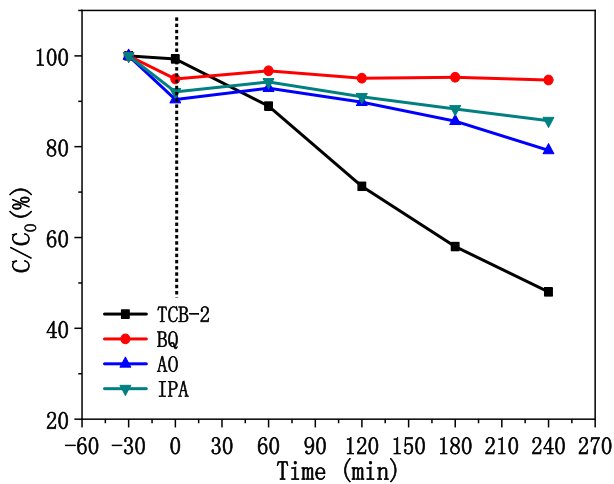


**Fig. 10** Trapping test of photogenerated holes and radicals in the photocatalytic system under visible light irradiation

**Table 1** The  $E_{CB}$ ,  $E_{VB}$ , and  $E_g$  for TiO<sub>2</sub>, g-C<sub>3</sub>N<sub>4</sub>, and Bi<sub>2</sub>O<sub>3</sub> at the point of zero charge

Material	$E_{CB}$ (eV)	$E_{VB}$ (eV)	$E_g$ (eV)
TiO <sub>2</sub>	- 0.28	2.90	3.18
g-C <sub>3</sub> N <sub>4</sub>	- 1.12	1.58	2.70
Bi <sub>2</sub> O <sub>3</sub>	0.33	3.13	2.80

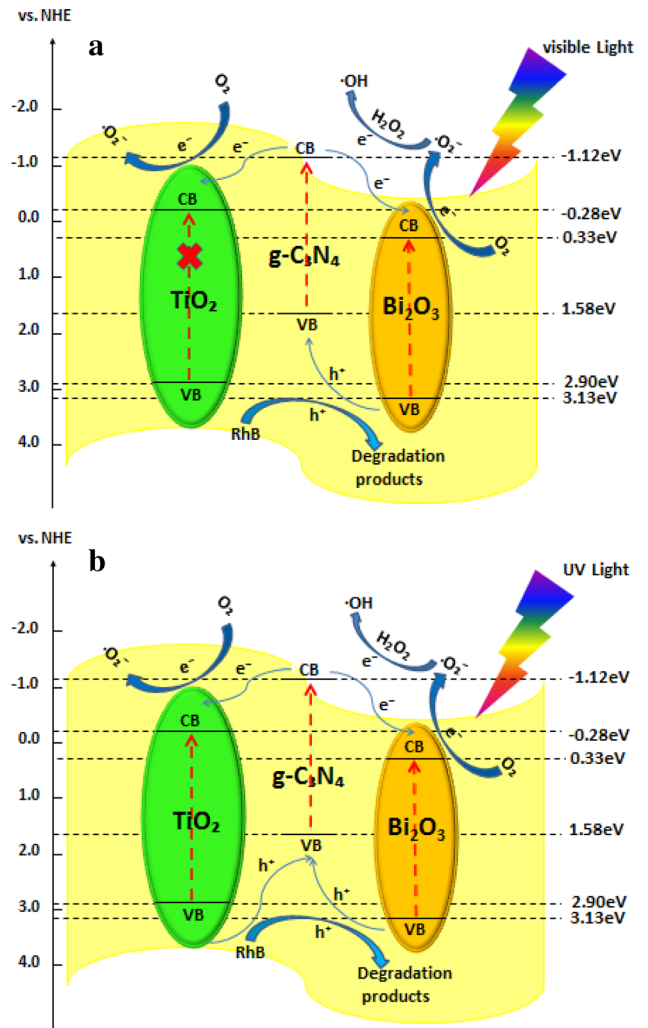


**Fig. 11** Mechanism of photocatalytic reaction of g-C<sub>3</sub>N<sub>4</sub>/Bi<sub>2</sub>O<sub>3</sub>/TiO<sub>2</sub> under **a** visible light and **b** UV light irradiation

Table 1, the separation of electron–hole pairs transferred better, but g-C<sub>3</sub>N<sub>4</sub> as the major part of hybrid had a weak response to UV and only a certain improvement for photocatalytic efficiency was obtained.

## 4 Conclusions

The multilayered heterojunction photocatalytic material g-C<sub>3</sub>N<sub>4</sub>/Bi<sub>2</sub>O<sub>3</sub>/TiO<sub>2</sub> was fabricated via microwave-assisted ball milling and the heat treatment method. This novel spatial structure facilitated electron transfer in the photocatalytic materials and the absorption ability in wide visible light range, and the entire photocatalytic system has achieved effectively separation of electron–hole pairs. It should be noted that in this study whether under visible or UV light to degrade RhB or MB, the photocatalytic effect of TCB is not satisfactory. This is probably a consequence of the photocatalytic selectivity of TCB and the change of the material crystal phase. The adsorption performance of composites to pollutants also affects the photocatalytic degradation ability. Notwithstanding its limitation, this study does suggest (1) The as-prepared material TCB boosts the separation and transfer of photogenerated charges at multilayer heterogeneous interfaces; (2) Scavenging experiments demonstrate that  $\cdot O_2^-$  radicals played a major role in photocatalytic degradation process; (3) The composites still have outstanding stability after using 5 times to degrade organic pollutants; (4) The red shift of the light absorption range of TCB indicates that the ability of hybrid materials to absorb visible light is enhanced facilitating the degradation of RhB or MB. This paper focuses on TCB photocatalytic performance for organic pollutants under visible light or UV irradiation, and provides relevant information for preparing novel ternary heterojunction photocatalytic materials.

## Acknowledgements

The work was supported by National Key Research and Development Program (No. 2018YFC1802605), Sichuan Provincial Major Science and Technology Project (No. 19ZDZX011), Nature Science Foundation of Sichuan Province (No. 2017SZ0181), International Cooperation Project of Sichuan Province (No. 2019YFH1027), Sichuan University-Yibin City school and City Strategic Cooperation Project (N0.2019 CDYB-26).

## Author contributions

CZ: Wrote the main manuscript text. WW: Performed the experiments. HH: Performed the experiments.

ZH: Analyzed the data. YW: Analyzed the data. JY: Review and editing.

## Compliance with ethical standards

**Conflict of interest** The authors declare that they have no known competing financial interests or personal relationships that could have appeared to influence the work reported in this paper.

## References

1. J. Yun, Y. Zhang, Y. Ren, P. Kang, J. Yan, W. Zhao, Z. Zhang, H. Guo, *Sol. Energy Mater. Sol. Cells* **210**, 110516 (2020)
2. K.T. Wong, S.C. Kim, K. Yun, C.E. Choong, I.W. Nah, B.H. Jeon, Y. Yoon, M. Jang, *Appl. Catal. B Environ.* **273**, 119034 (2020)
3. M. Jourshabani, B.K. Lee, Z. Shariatinia, *Appl. Catal. B Environ.* **276**, 119157 (2020)
4. J. Su, L. Zhu, P. Geng, G. Chen, *J. Hazard. Mater.* **316**, 159 (2016)
5. N. Guo, Y. Zeng, H. Li, X. Xu, H. Yu, X. Han, *J. Hazard. Mater.* **353**, 80 (2018)
6. R. Hao, G. Wang, H. Tang, L. Sun, C. Xu, D. Han, *Appl. Catal. B Environ.* **187**, 47 (2016)
7. A.L. Linsebigler, G. Lu, J.T. Yates, *Chem. Rev.* **95**, 735 (1995)
8. S. Lakshmi, R. Renganathan, S. Fujita, *J. Photochem. Photobiol. A Chem.* **88**, 163 (1995)
9. B. Jürgens, E. Irran, J. Senker, P. Kroll, H. Müller, W. Schnick, *J. Am. Chem. Soc.* **125**, 10288 (2003)
10. D.A. Solís-Casados, L. Escobar-Alarcón, A. Arrieta-Castañeda, E. Haro-Poniatowski, *Mater. Chem. Phys.* **172**, 11 (2016)
11. Y. Liu, F. Xin, F. Wang, S. Luo, X. Yin, *J. Alloys Compd.* **498**, 179 (2010)
12. K. Hu, R. Li, C. Ye, A. Wang, W. Wei, D. Hu, R. Qiu, and K. Yan, *J. Clean. Prod.* **253**, (2020).
13. Y. Sheng, Z. Wei, H. Miao, W. Yao, H. Li, Y. Zhu, *Chem. Eng. J.* **370**, 287 (2019)
14. X. Chen, J. Wei, R. Hou, Y. Liang, Z. Xie, Y. Zhu, X. Zhang, H. Wang, *Appl. Catal. B Environ.* **188**, 342 (2016)
15. F. Bairamis, I. Konstantinou, D. Petrakis, and T. Vaimakis, *Catalysts* (2019).
16. P. Mei, H. Wang, H. Guo, N. Zhang, S. Ji, Y. Ma, J. Xu, Y. Li, H. Alsulami, M.S. Alhodaly, T. Hayat, Y. Sun, *Environ. Res.* **182**, 109090 (2020)
17. R. Zhang, Y. Yu, H. Wang, J. Du, *Sci. Total Environ.* **724**, 138280 (2020)

18. R. Acharya, K. Parida, *J. Environ. Chem. Eng.* **8**, 103896 (2020)
19. M.B. Tahir, M. Sagir, K. Shahzad, *J. Hazard. Mater.* **363**, 205 (2019)
20. C. Li, Z. Sun, W. Zhang, C. Yu, S. Zheng, *Appl. Catal. B Environ.* **220**, 272 (2018)
21. Y. Zhang, J. Lu, M.R. Hoffmann, Q. Wang, Y. Cong, Q. Wang, H. Jin, *RSC Adv.* **5**, 48983 (2015)
22. L. Li, B. Yan, *J. Alloys Compd.* **476**, 624 (2009)
23. S. Anandan, G.J. Lee, P.K. Chen, C. Fan, J.J. Wu, *Ind. Eng. Chem. Res.* **49**, 9729 (2010)
24. W. Li, D. Li, Y. Lin, P. Wang, W. Chen, X. Fu, Y. Shao, *J. Phys. Chem. C* **116**, 3552 (2012)
25. C. Pan, Y. Yan, H. Li, S. Hu, *Adv. Mater. Res.* **557–559**, 615 (2012)
26. G. Ren, X. Ren, W. Ju, Y. Jiang, M. Han, Z. Dong, X. Yang, K. Dou, B. Xue, F. Li, *J. Photochem. Photobiol. A Chem.* **392**, 112367 (2020)
27. J. Hu, H. Li, C. Huang, M. Liu, X. Qiu, *Appl. Catal. B Environ.* **142–143**, 598 (2013)
28. Y. Wang, J. Yu, W. Peng, J. Tian, C. Yang, *Sci. Rep.* **9**, 1 (2019)
29. S.H. Hsieh, A. Manivel, G.J. Lee, J.J. Wu, *Mater. Res. Bull.* **48**, 4174 (2013)
30. X. Yao, X. Liu, *J. Hazard. Mater.* **280**, 260 (2014)
31. Q. Hao, R. Wang, H. Lu, C. Xie, W. Ao, D. Chen, C. Ma, W. Yao, Y. Zhu, *Appl. Catal. B Environ.* **219**, 63 (2017)
32. H. Cheng, B. Huang, J. Lu, Z. Wang, B. Xu, X. Qin, X. Zhang, Y. Dai, *Phys. Chem. Chem. Phys.* **12**, 15468 (2010)
33. P. Kumar, P. Kar, A.P. Manuel, S. Zeng, U.K. Thakur, K.M. Alam, Y. Zhang, R. Kisslinger, K. Cui, G.M. Bernard, V.K. Michaelis, *Adv (Opt, Mater)*, 2020).
34. J. Matos, R. Montaña, E. Rivero, A. Escudero, D. Uzcategui, *Water Sci. Technol.* **69**, 2184 (2014)
35. W. Xiaohong, Q. Wei, H. Weidong, *J. Mol. Catal. A Chem.* **261**, 167 (2007)
36. X. Li, G. Hartley, A.J. Ward, P.A. Young, A.F. Masters, T. Maschmeyer, *J. Phys. Chem. C* **119**, 14938 (2015)
37. P.Y. Kuang, Y.Z. Su, G.F. Chen, Z. Luo, S.Y. Xing, N. Li, Z.Q. Liu, *Appl. Surf. Sci.* **358**, 296 (2015)
38. X. Dong, Z. Sun, X. Zhang, C. Li, S. Zheng, *J. Taiwan Inst. Chem. Eng.* **84**, 203 (2018)
39. P. Zhang, C. Shao, M. Zhang, Z. Guo, J. Mu, Z. Zhang, X. Zhang, Y. Liu, *J. Hazard. Mater.* **217–218**, 422 (2012)
40. K. Su, Z. Ai, L. Zhang, *J. Phys. Chem. C* **116**, 17118 (2012)
41. Y. Cui, H. Zhang, R. Guo, Q. Ma, X. Deng, X. Cheng, X. Li, M. Xie, Q. Cheng, C. Zou, *Electrochim. Acta* **246**, 1075 (2017)
42. Y. Gun, G.Y. Song, V.H.V. Quy, J. Heo, H. Lee, K.S. Ahn, S.H. Kang, *A.C.S. Appl. Mater. Interfaces* **7**, 20292 (2015)
43. J. Zhang, Y. Hu, X. Jiang, S. Chen, S. Meng, X. Fu, *J. Hazard. Mater.* **280**, 713 (2014)
44. T. Chen, Q. Hao, W. Yang, C. Xie, D. Chen, C. Ma, W. Yao, Y. Zhu, *Appl. Catal. B Environ.* **237**, 442 (2018)
45. C. Wang, C. Shao, L. Wang, L. Zhang, X. Li, Y. Liu, *J. Colloid Interface Sci.* **333**, 242 (2009)
46. Y. Wang, Y. Wen, H. Ding, Y. Shan, *J. Mater. Sci.* **45**, 1385 (2010)
47. S. Chen, Y. Hu, S. Meng, X. Fu, *Appl. Catal. B Environ.* **150–151**, 564 (2014)
48. W.K. Jo, T.S. Natarajan, *Chem. Eng. J.* **281**, 549 (2015)

**Publisher's Note** Springer Nature remains neutral with regard to jurisdictional claims in published maps and institutional affiliations.